Particle simulation model of transport in a bounded, Coulomb collisional plasma

Richard J. Procassini and Charles K. Birdsall

Particle simulation model of transport in a bounded, Coulomb collisional plasma

Richard J. Procassini[a] and Charles K. Birdsall

Electronics Research Laboratory, University of California, Berkeley, California 94720

The transport of particles and energy in a fully ionized, collisional plasma is studied through the use of a kinetic transport model. A particle-in-cell (PIC) code has been coupled to a Monte Carlo, binary particle model of Coulomb collisions, to provide a fully kinetic, self-consistent description of transport and potential formation in a single spatial dimension and two velocity components (parallel and perpendicular to the spatial coordinate). The dependence of plasma transport on Coulomb collisionality is investigated by varying the normalized collision frequency within the range $10^{-2} \leqslant \nu_* \equiv \nu_{c0}/\nu_{be0} \leqslant 5$, where ν_{c0} is the average electron/ion collision frequency and ν_{be0} is the frequency at which thermal electrons bounce between the collector sheath potential drops located adjacent to the absorbing plates at each end of the system. Collisions between charged-plasma and recycled-neutral particles are omitted in this study. For finite values of ν_*, the heat conduction flux is found to be reduced from the value predicted by classical, hydrodynamic transport theory. The electron heat conduction flux is shown to lie between 12% and 21% of the free-streaming thermal flux $q_{fs}^e \equiv n_e \nu_{\parallel,te} k T_e$, where n_e, $\nu_{\parallel,te}$, and $k T_e$ are the steady-state values of the electron density, parallel thermal velocity, and temperature, respectively. The variation of several transport quantities with collisionality is presented, and the results are compared against those from other collisional plasma transport models.

I. INTRODUCTION

The transport of particles and energy within a bounded, Coulomb collisional plasma is an important topic in many areas of plasma physics. These include issues related to the power and particle exhaust from the edge region of fusion plasmas,[1,2] plasma diagnostic methods that are based upon intrusive probes,[3,4] and the plasma–surface interactions that are the essence of plasma-assisted materials processing.[5,6] Hydrodynamic transport theory[7-10] has been extensively employed in the analysis of particle and energy transport in a Coulomb collisional plasma.[11-13] As an alternative to the use of these fluid models, in this paper we present the results of a study in which kinetic particle-in-cell (PIC) techniques are employed to simulate transport in a collisional plasma. This model combines standard PIC techniques with a Monte Carlo description of Coulomb collisions. The use of a kinetic model is motivated by the limitations of the fluid description of collisional plasma transport, which are discussed in Sec. II. The kinetic transport model that is used for this study is described in Sec. III. The PIC model is used to determine the dependence of various transport quantities on collisionality. The results of this study are presented in Sec. IV. Comparison is made with the results of other plasma transport models in Sec. V. The conclusions of the present study are discussed in Sec. VI.

II. MOTIVATION FOR THE USE OF A KINETIC DESCRIPTION OF TRANSPORT IN A BOUNDED, COLLISIONAL PLASMA

Hydrodynamic descriptions of collisional plasma transport are based upon assumptions that may not be valid over a wide range of Coulomb collisionality or in the collector sheath region adjacent to a plasma boundary. The limitations on the use of classical transport theory, and the relevant physics of the sheath region, are briefly reviewed. The applicability of fluid models to the study of transport in a bounded, collisional plasma is also discussed.

A. A review of classical (hydrodynamic) transport models

The fluid-equation plasma transport theory developed by Spitzer and Härm,[7] and Braginskii[8] is based upon a linear perturbation of the Fokker–Planck kinetic equation

$$\frac{\partial f}{\partial t} + \mathbf{v} \cdot \frac{\partial f}{\partial \mathbf{x}} + \mathbf{a} \cdot \frac{\partial f}{\partial \mathbf{v}} = C(f,f), \tag{1}$$

where t is time, $\mathbf{x}$ is position, $\mathbf{v}$ is velocity, $\mathbf{a}$ is acceleration, $f(\mathbf{x},\mathbf{v},t)$ is the particle distribution function, and $C(f,f)$ represents the time rate of change of f arising from Coulomb collisions. The distribution function is expanded with regard to its velocity dependence, and only the first two terms are retained,

$$f(v) = f_0(v) + f_1(v), \tag{2}$$

where for highly collisional plasmas $f_0(v)$ is assumed to be Maxwellian and $f_1(v) \ll f_0(v)$ is the non-Maxwellian contribution to the distribution function. The transport coefficients, i.e., resistivity, viscosity, and conductivity, are obtained from the non-Maxwellian component f_1.

The perturbed component of the distribution function $f_1(v)$ is proportional to spatial gradients of the temperature (T) and electrostatic potential (ϕ),[7]

$$f_1(v) \sim f_0(v)[\mathscr{D}_T(v) + \mathscr{D}_\phi(v)], \tag{3}$$

where the functions $\mathscr{D}_T(v)$ and $\mathscr{D}_\phi(v)$ have the form[14,7]

$$\mathscr{D}_T(v) \sim \lambda \nabla_\parallel T/T, \tag{4}$$

$$\mathscr{D}_\phi(v) \sim \lambda \nabla_\parallel \phi/T, \tag{5}$$

with $\lambda \equiv v_t/v_c$ is the collisional mean-free path, $v_t = (kT/m)^{1/2}$ is the particle thermal velocity, and v_c is the Coulomb collision frequency. This form of the perturbed distribution function $f_1(v)$, which in general is asymmetric with regard to zero velocity, leads to finite values of the plasma current $[J \equiv \int Zev f_1(v) d^3v]$ and the heat flux $[q \equiv \int \epsilon v f_1(v) d^3v$, where Ze is the charge and $\epsilon \equiv mv^2/2$ the kinetic energy of the particles]. Therefore particle and energy tranport is a result of the formation of temperature and potential gradients in the plasma.

The classical plasma transport equations of Braginskii[8] are derived by inserting the linearized distribution function (2) into the kinetic equation (1), keeping only those terms that are linear in f_1, and taking the first three velocity moments of the resulting equation. One then obtains

$$\frac{\partial n_s}{\partial t} + \nabla \cdot (n_s \mathbf{u}_s) = 0,$$

$$m_s n_s \left(\frac{\partial \mathbf{u}_s}{\partial t} + (\mathbf{u}_s \cdot \nabla) \mathbf{u}_s \right) - q_s n_s \left(\mathbf{E} + \frac{1}{c} \mathbf{u}_s \times \mathbf{B} \right)$$
$$= -\nabla p_s - \nabla \cdot \Pi + \mathbf{R}_c,$$

$$\frac{3}{2} n_s \left(\frac{\partial T_s}{\partial t} + (\mathbf{u}_s \cdot \nabla) T_s \right) + p_s \nabla \cdot \mathbf{u}_s$$
$$= -\nabla \cdot \mathbf{q}_s - (\Pi \cdot \nabla) \mathbf{u}_s + Q_s, \tag{6}$$

where the subscript s represents the species, m is mass, n is density, c is the speed of light, $\mathbf{u} = \int v f(v) d^3v$ is the mean fluid velocity, $p = nT$ is the isotropic scalar pressure at temperature T, Π is the nonisotropic position of the stress tensor, $\mathbf{E}$ and $\mathbf{B}$ are the electric and magnetic field strengths, $\mathbf{R}_c$ is the mean change in the particle momentum of the given species arising from collisions with particles of all other species, $\mathbf{q}$ is the conduction heat flux, and Q is the heat generated in particles of the given species arising from collisions with particles of all other species. Equations (6) are the conservation equations for the number of particles, momentum, and flow energy.

The perturbative expansion (2) is only valid for highly collisional plasmas, such that f_0 is maintained a Maxwellian distribution. This implies low to moderate energies, since the Coulomb collision frequency is defined as

$$v_{c0} \equiv 4\pi q_\alpha^2 q_\beta^2 n_\beta \ln(\Lambda)/\mu^2 v_{rel}^3, \tag{7}$$

where $\ln(\Lambda)$ is the Coulomb logarithm, μ is the reduced mass, and v_{rel} is the relative velocity of particles α and β. An estimate of the collisionality is given by the ratio of the collisional mean-free path λ to the temperature scale length $L_T \equiv |(1/T)(\partial T/\partial z)|^{-1}$. The validity of the perturbation expansion breaks down for $\lambda/L_T \gtrsim 0.1$, which may be exceeded by high-energy electrons in a collisional plasma. An accurate description of collisional transport by high-energy particles therefore requires either a *kinetic* treatment, or a model that includes additional terms in the expansion of the distribution function (2).[10]

B. A review of collector sheath physics

For the purposes of the present study, it is assumed that the collisional plasma is bounded by an absorbing, electrostatically floating conductor. A negative net charge is maintained on the surface of this bounding plate, because, during the transient phase of the discharge, the more mobile electrons arrive prior to the ions. This generates a potential structure in the region adjacent to the plate that decreases monotonically toward the plate. This *collector sheath* accelerates the ions and reflects a fraction of the electrons that are incident upon it. The net effect is an equilibration of the electron and ion currents at the plate.

The ions that strike the plate, having been accelerated by the sheath, may be energetic enough to sputter neutral atoms from the plate. If the sputtering rate exceeds the redeposition rate, net erosion of the plate occurs. While this process is desirable for certain applications, such as plasma etching of semiconductor materials,[15,16] it can be detrimental in others. A case in point is the sputtering of limiters or divertor plates in the edge region of a tokamak fusion device.[17,18] A net erosion rate reduces the lifetime of these plasma-facing components and is a major source of impurities that can lead to radiative cooling of the ignited core plasma. In this case, it is desirable to have a collector sheath potential drop that is as small as possible, to reduce the kinetic energy with which the ions impact the plate.

The collector sheath potential drop reduces the electron density relative to the ion density, such that the sheath region is highly *non-neutral* and relatively *collisionless* [see Eq. (7)]. The acceleration of particles by the presheath and collector sheath leads to velocity distributions that have large *non-Maxwellian* components. Therefore the assumption made in the derivation of classical transport theory (i.e., nearly Maxwellian velocity distributions that are maintained by large Coulomb collisionality) is not strictly valid in the collector sheath region. Many hydrodynamic transport models also assume that the plasma is quasineutral. Therefore an accurate description of particle and energy transport in the collector sheath region requires a *kinetic* treatment.

III. DESCRIPTION OF THE KINETIC TRANSPORT MODEL

The computational tool used for this study is the electrostatic PIC code DIPSI (Direct Implicit Plasma–Surface Interactions).[19] While the PIC methodology forms the basis of the kinetic transport model, the code is enhanced by the addition of (see Ref. 20) (i) a self-consistent, relativistic, Monte Carlo binary collision model, (ii) a distributed source injection model, and (iii) neutral-particle charge exchange and impact ionization models (these are not used in the present study, which is concerned only with transport arising from Coulomb collisions in a fully ionized plasma).

The single-spatial-dimension PIC model that is used for this study is shown in Fig. 1, including the symmetry midplane, the floating collector plate, and a typical electrostatic potential structure. The computational domain is divided into three regions: the source region $0 \leqslant z \leqslant L_S$ (region I), the source-free region $L_S \leqslant z \leqslant z^*$ (region II), and the collector
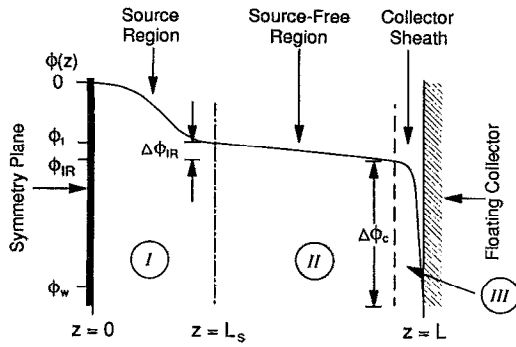
FIG. 1. The one-dimensional particle-in-cell model of a bounded, collisional plasma system showing a characteristic potential profile in the source region (I), source-free region (II), and collector sheath region (III).

sheath region $z^* \leqslant z \leqslant L$ (region III). Note that, in general, regions I and II may be replaced by a single source region that extends over the range $0 \leqslant z \leqslant z^*$. The system shown in Fig. 1 was chosen in order to separate out the contributions to the potential variation that arise from source and collisional effects.

A. The particle-in-cell model

The PIC model that forms the core of the kinetic transport model advances the trajectories of charged simulation particles in a single spatial dimension ($\hat{z}$) and two velocity components ($v_\parallel$ and $v_\perp$) according to the guiding-center equations of motion,

$$\frac{dz}{dt} = v_\parallel, \tag{8}$$

$$\frac{dv_\parallel}{dt} = \frac{q}{m} E_\parallel - \frac{\mu}{m} \nabla B_\parallel + \left(\frac{dv_\parallel}{dt}\right)_{\text{coll}}, \tag{9}$$

$$\frac{d\mu}{dt} = \left(\frac{d\mu}{dt}\right)_{\text{coll}}, \tag{10}$$

where z is the axial position, t is the time, $\mu \equiv \frac{1}{2}mv_\perp^2/B_0$ is the magnetic moment, m and q are the particle mass and charge, and $E_\parallel$ and $B_\parallel$ are the electric and magnetic fields along the spatial coordinate. A direct-implicit scheme[21,22] is used to integrate (8)–(10) in time. The ambipolar, electrostatic potential is calculated via the direct-implicit form of Poisson's equation,

$$-\nabla \cdot \left(1 + \sum_s \chi_s\right) \nabla \Phi(z) = 4\pi e [Zn_i(z) - n_e(z)], \tag{11}$$

where the sum is over species s (ions and electrons), n_s is the free-streaming or explicit density, and χ_s is the implicit susceptibility, which is the implicit correction to the free-streaming charge density. Equations (8)–(11) are solved via standard finite-difference techniques.

B. The distributed source injection model

Particles are assumed to enter the system in the distributed source region (I) as electron–ion pairs. This ensures that the system will remain globally quasineutral. The source function used in the particle injection model is that of Emmert et al.,[23]

$$S_s(z,v_d) = R_{\text{inj}}^s h(z)(m_s v_d/kT_{ds0})$$
$$\times \exp(-m_s v_d^2/2kT_{ds0}), \tag{12}$$

where the subscripts d and s represent the directional components ($\parallel$ or $\perp$) and the species (electrons or ions), respectively, R_{inj}^s is the total injection rate for particles of species s, $h(z)$ is the normalized injection profile, i.e., $(1/L_s)\int_0^{L_s} h(z')dz' = 1$, and kT_{ds0} is the source temperature for species s in direction d. Both the ions and electrons are injected via this model, which was chosen because it produces distribution functions $f(z,v_d)$, which are Maxwellian in the absence of any electric fields.[24]

Once particles are injected into the system, they flow along magnetic field lines that are oriented parallel (normal) to the $\hat{z}$ axis (plate at $z = L$). The magnetic field intensity is assumed to be constant along the $\hat{z}$ axis, such that the second term on the right side of (9) is zero. Particles that cross the symmetry midplane located at $z = 0$ are specularly reflected: $-z \rightarrow z$ and $-v_\parallel \rightarrow v_\parallel$. This process conserves the momentum and kinetic energy of the reflected particle. Particles that are incident upon the collector plate (i.e., all of the ions and the "energetic" electrons) are absorbed on the surface of the plate. Ion and electron reflection, in either a charged or neutral state, and secondary electron emission, are not included in this study. The charge of the absorbed particles is added to the net plate surface charge, hence the plate potential floats electrostatically.

C. The Monte Carlo Coulomb collision model

The collision package that is incorporated into the kinetic transport model employs Monte Carlo techniques to simulate the pitch-angle scattering of the plasma particles. It is similar in operation to the model developed by Takizuka and Abe.[25] Since the transport model has only a single spatial dimension (with three velocity components), it is not possible to simulate the details of Coulomb scattering based upon impact parameters. However, it is possible to scatter a particle's velocity through an angle θ that is chosen randomly from an appropriate distribution of angles. The mean scattering angle of the distribution is zero, and the variance of the distribution is given (for an electron–ion collision) by[26,20]

$$\langle \theta^2 \rangle = (v_{\text{th}}/v_{\text{rel}})^3 (n_{\text{loc}}/n_{\text{ave}}) v_{c0} \Delta t, \tag{13}$$

where v_{th} is the thermal velocity of the incident particle, v_{rel} is the relative velocity of the colliding particles, n_{loc} and n_{ave} are the local and average particle densities, v_{c0} is the average electron–ion collision frequency, and Δt is the simulation time step. Therefore the angle θ is determined from the global collision frequency, as modified for local variations in the plasma temperature and density [see Eq. (7)].

The model only allows collisions between particles within a given spatial grid cell. The interacting particles are scattered off of one another without regard for the distance between their midpoints. Particles undergo the full range of Coulomb collisional interactions: electron–electron, electron–ion, and ion–ion collisions are all included. This colli-

sion algorithm conserves the momentum and energy of the interacting particles.[20] Conservation of these quantities is important if one wants to maintain the correct collisional energy balance in the plasma. Collisions occur everywhere *except* the collector sheath region (region III). The reason for this is twofold. First, the sheath region is not as collisional as the other regions in the plasma because the electron density (and hence the collision frequency) there is reduced by the decreasing potential structure. Second, since the collisional mean-free path (λ) is usually much larger than the electron Debye length (λ_{De}, the scale length over which the collector sheath forms), there are only a small number of collisions taking place in the region.

IV. PARTICLE SIMULATIONS OF TRANSPORT IN A BOUNDED, COLLISIONAL PLASMA

The physical parameters that are used as input to the previously described particle simulation model of collisional transport are presented, followed by a detailed discussion of the results of the study.

A. Simulation parameters

The system is initially loaded with a uniform, low-density plasma. Particles are injected into the source region $0 \leqslant z \leqslant L_S$ (region I) to balance the loss of plasma to the bounding plate. The plasma densities, temperatures, and potential come to equilibrium when the particle creation and loss rates balance.

For this study, a basic system was chosen with specific values of the length (L), particle injection rate (R_{inj}), source temperatures (kT_0), equilibrium density (n_{eq}), and mass ratio (m_e/m_i). The average or global collision frequency (ν_{c0}), which is an input parameter for this model, was varied over a number of simulations, so as to span a wide range of collisionality. The basic bounded, collisional plasma system is described by the quantities listed in Table I.

Seven simulations were performed, varying the global electron–ion collision frequency ν_{c0} over the range $0.01\nu_{bc0} \leqslant \nu_{c0} \leqslant 5.0\nu_{bc0}$, where $\nu_{bc0} \equiv v_{te0}/L$ is the source electron bounce frequency, and v_{te0} is the source electron thermal velocity. The process of varying the collisionality $\nu^* \equiv \nu_{c0}/\nu_{bc0}$ (the notation used herein has been borrowed from the paper by Takizuka, *et al.*[27]) for a system with a fixed number of Debye lengths λ_{De0} allows one to change the collisional mean-free path λ while maintaining a constant system length L. This effectively uncouples the physical and "collisional" densities.

When the collision frequency is "accelerated" while the system length is held constant, care must be taken to ensure that the relative scaling of the collisional mean-free path to the electron Debye length (i.e., $\lambda/\lambda_{De} \gg 1$) is maintained. The mean-free path should not be reduced to the order of, or smaller than, the Debye length. In the seven simulations described above, the ratio of the mean-free path to the electron Debye length was in the range $6550 \gtrsim \lambda_{e/e}/\lambda_{De} \gtrsim 12$ for collisionalities in the range $0.01 \leqslant \nu^* \leqslant 5$, such that $\lambda_{e/e}/\lambda_{De} \gg 1$ is satisfied in each of the simulations.

The kinetic PIC model is capable of providing a self-consistent description of collisional transport *and* potential formation in a bounded plasma system over a wide range of spatial and temporal scales. However, an accurate calculation of the potential structure (and subsequently, particle and energy transport) in the non-neutral sheath region requires adequate resolution of the electron Debye length λ_{De} and plasma period ω_{pe} over the entire system. Therefore the simulations were run in the explicit limit with $\omega_{pe0} \Delta t = 0.20$ and $\Delta z/\lambda_{De0} = 0.50$, where Δt and Δz are the time step and grid spacing, respectively.

Note that the mass ratio is reduced relative to that for hydrogen ($m_H/m_e = 1836$). This will produce a total potential drop ϕ_w that is smaller and a mean flow velocity $\langle v \rangle$ that is larger than those for hydrogen.[28] Each simulation was run to equilibrium in four thermal-ion transit times $T_{tot} = 4L/v_{ti0}$, where v_{ti0} is the source ion-thermal velocity. Depending upon the system collisionality (which is discussed below), the final simulation time T_{tot} lies in the range $0.6 \lesssim T_{tot}/\tau_0^{e/e} \lesssim 284$ ($0.04 \lesssim T_{tot}/\tau_0^{i/i} \lesssim 20$), where $\tau_0^{e/e}$ ($\tau_0^{i/i}$) is the basic collision time for source electrons (ions). The basic collision time τ_0 is defined as the reciprocal of the basic collision frequency ν_{c0}, which is given by (7).

The number of particles per grid cell at equilibrium was $N_{cell} \simeq 100$ (or $N_{De} \simeq 200$ particles per Debye length) for each simulation. This results in $\sim 10\%$ statistical error in the value of quantities that are defined on the grid. This density of simulation particles (which are also known as *superparticles*) was chosen for two reasons: (i) it has been shown that superparticle densities on this order are required to produce accurate potential profiles in the quasineutral region of the plasma;[29] and (ii) it is desirable to minimize the level of velocity-space diffusion arising from potential fluctuations, which increase the total collisionality of the system.[30] Simulations using a PIC code that is similar to that described herein have produced inconsistent results (which will be discussed in detail below) when the superparticle density was only $N_{cell} \simeq 12$ particles per cell.[27]

Many plasma applications operate within the aforementioned range of collisionality. In the area of fusion plasmas, the Japanese tokamak JT-60 (Ref. 27) operates with the scrapeoff layer plasma of length $L \simeq 5 \times 10^3$ cm in either a low-density, high-temperature mode ($n_e \simeq 10^{12}$ cm^{-3} and $kT_e \simeq 200$ eV) with $\nu^* \simeq 0.5$, or a high-density, low-temperature mode ($n_e \simeq 10^{13}$ cm^{-3} and $kT_e \simeq 90$ eV) such that $\nu^* \simeq 21.8$. In the area of plasma-assisted materials processing,[31] etching reactors of length $L \simeq 50$ cm operate with densities and temperatures in the range $n_e \simeq 10^9 - 10^{12}$ cm^{-3} and $kT_e \simeq 1-10$ eV, such that $\nu^* \simeq 2.0 \times 10^{-7} - 2.0 \times 10^{-2}$. It is

TABLE I. Simulation parameters used to model transport in a bounded, collisional plasma.

System length:	$L = 65\lambda_{De0} = 0.216$ cm
Source region width:	$L_S = 0.3L = 0.0648$ cm
Particle injection rate:	$R_{inj} = 2.8$ particles pairs per Δt
Electron source temperature:	$kT_{\parallel,e0} = kT_{\perp,e0} = 100$ eV
Ion source temperature:	$kT_{\parallel,i0} = kT_{\perp,i0} = 100$ eV
Equilibrium density:	$n_{eq} = 5.0 \times 10^{12}$ cm^{-3}
Mass ratio:	$m_i/m_e = 200$

important to note that the high-energy electrons in the tail of a Maxwellian distribution, which carry the majority of the heat through the collisional plasma,[28,32] are much less collisional than the values for thermal electrons listed above.

B. Characteristic results of the system at equilibrium

The profiles of the electrostatic potential and various moments of particle distribution functions obtained from a simulation with a normalized, global collision frequency $\nu^* = 1$ are shown in Fig. 2. The time-averaged, velocity-space density contours of the electrons and ions obtained from the same simulation are presented in Figs. 3 and 4, respectively. Each of these equilibrium profiles and velocity distributions is described below.

1. The electrostatic potential

The total ambipolar potential drop ϕ_w shown in Fig. 2(a) is a sum of the source sheath drop $\Delta\phi_1$ (which develops, in large part, because the electrons injected into region I have a larger thermal velocity than the injected ions), the collisional presheath drop within the source-free region (region II) $\Delta\phi_{IR}$ (which leads to transport along the spatial coordinate) and the collector sheath drop $\Delta\phi_c$ in region III. It turns out that the source presheath potential drop $\Delta\phi_1$ is the sum of the potential variation arising from the injected flux imbalance *and* the collisional interactions within region I. The collisional presheath drop in the source-free region (region II) will increase as the ratio of the collisional mean-free path to the system length λ/L is decreased (either by
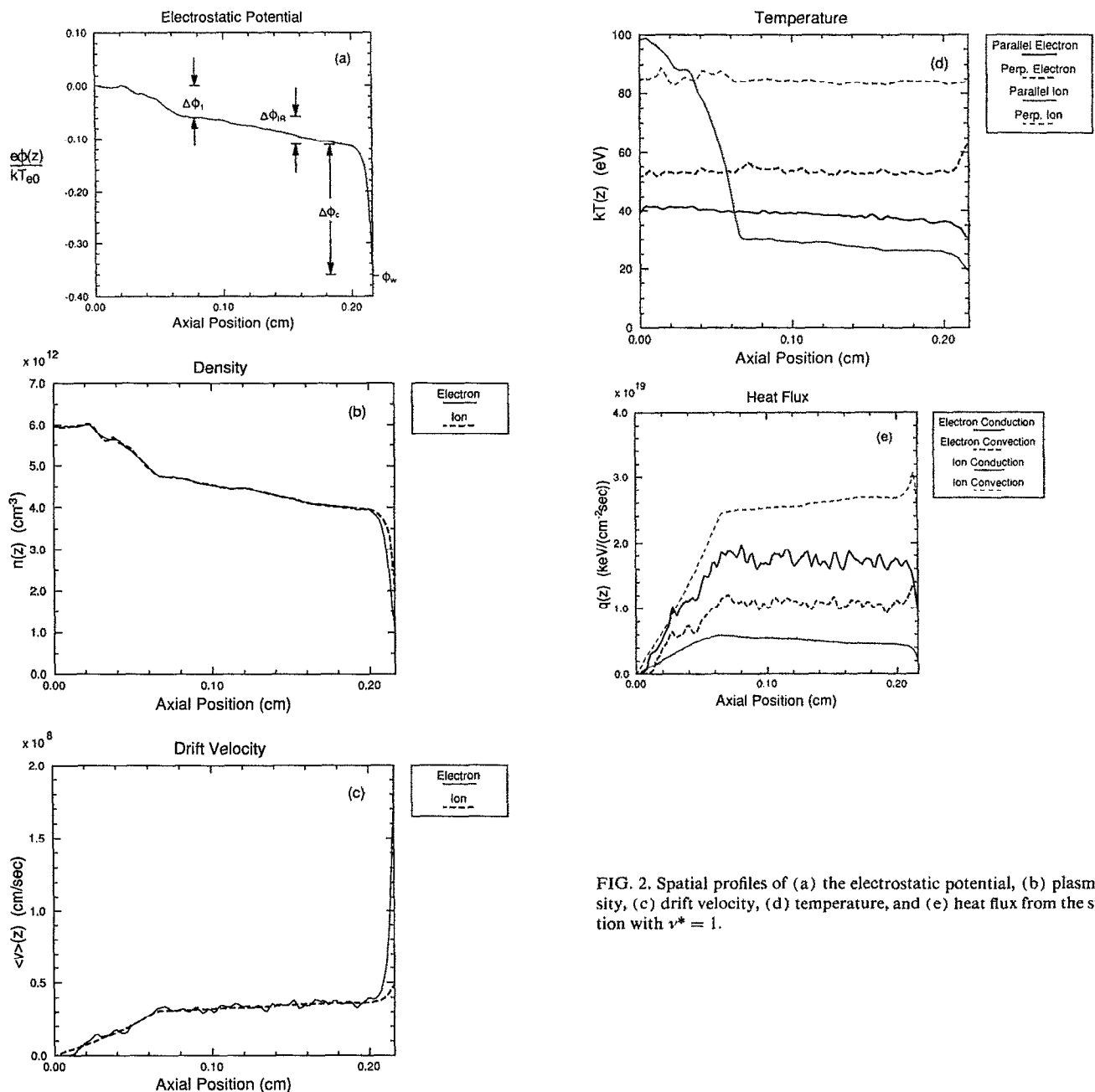

FIG. 2. Spatial profiles of (a) the electrostatic potential, (b) plasma density, (c) drift velocity, (d) temperature, and (e) heat flux from the simulation with $\nu^* = 1$.
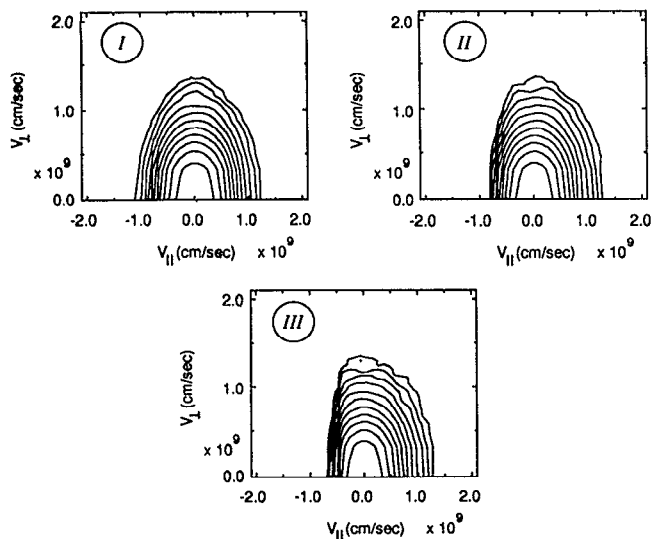
FIG. 3. Time-averaged, velocity-space density contour plots of the electrons in the source region (I), source-free region (II), and collector sheath region (III) from the simulation with $\nu^* = 1$.

decreasing λ for a fixed L, or increasing L for a fixed value of λ), since the resistance per unit length increases.

2. Plasma density

The density (the zeroth moment of f) profiles of Fig. 2(b) indicate that the system is quasineutral ($n_e \simeq n_i$) outside the collector sheath region ($0 \leqslant z \lesssim 0.20$ cm), where the electron density is reduced relative to the ion density ($n_i > n_e$) by the rapidly decreasing potential structure in the sheath region.

3. Plasma flow velocity

The drift or flow velocity (the first moment of f) profiles of the electrons and ions are presented in Fig. 2(c). Outside
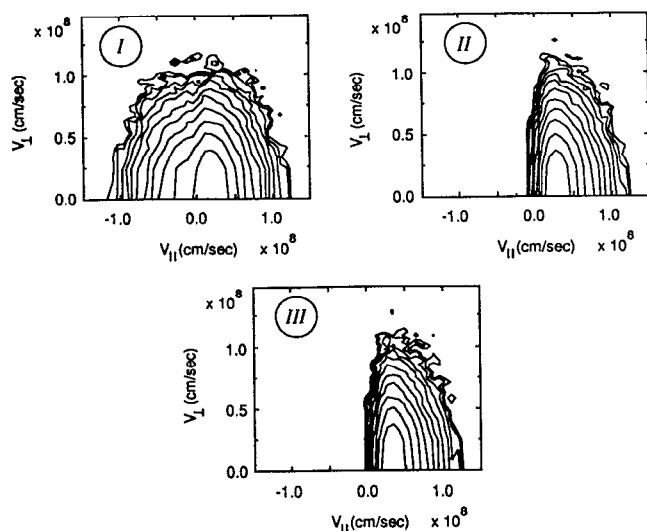

FIG. 4. Time-averaged, velocity-space density contour plots of the ions in the source region (I), source-free region (II), and collector sheath region (III) from the simulation with $\nu^* = 1$.

the collector sheath region, the electrons and ions are flowing toward the plate at about the same speed. All the ions are accelerated in the direction of the plate by the collector sheath drop, as shown in the figure. The large increase in the electron drift velocity in this region arises because only the most energetic electrons are able to traverse the collector sheath region and impact the plate.

4. Plasma temperature

The parallel and perpendicular temperature (the variance of the second moment of f) profiles of the electrons and ions are shown in Fig. 2(d). While both species are injected into the system with equal and isotropic source temperatures ($kT_{\parallel,e0} = kT_{\perp,e0} = kT_{\parallel,i0} = kT_{\perp,i0} = 100$ eV), the equilibrium temperatures are nonisotropic and smaller than the source temperature. The parallel electron temperature is reduced because the energetic electrons in the tail of the distribution are lost due to absorption on the plate. The perpendicular components of the temperature (especially that of the electrons) are reduced via collisional energy transfer to the parallel components. The large falloff in the parallel ion temperature near $z = L_S = 0.065$ cm is due to the discontinuity at that location between the full-Maxwellian distribution (in the absence of any perturbing electric fields) in the source region $0 \leqslant z \leqslant L_S$ and the right-going half-Maxwellian distribution for $z > L_S$. Since the ion distribution has the same form $\sim \exp[-v^2/(2v_{ti0}^2)]$ on either side of $z = L_S$, Schwager and Birdsall[29] show that the effective thermal velocity of the half-Maxwellian distribution becomes $v_{ti*} = [1 - 2/\pi]^{1/2} v_{ti0}$, such that $T_{\parallel,i}(z > L_S) \simeq 0.363 T_{\parallel,i0}$. At $z = L_S$, the measured parallel ion temperature is $T_{\parallel,i}(z = L_S) = 0.301 T_{\parallel,i0} = 30.1$ eV, which is smaller than the value predicted by the theory of Schwager and Birdsall because the distribution is cooled as the ions are accelerated by the source sheath potential drop.

5. Plasma heat flux

The total kinetic energy flux (which is derived from the third moment of f) is comprised of a conduction component (arising from collisional interactions) and a convection component (due to the flow of thermal energy at the drift velocity). Figure 2(e) indicates that the electron conduction flux dominates that of the ions, as a result of the larger electron collision frequency. Conversely, the convection of thermal energy by the ions is larger than that for the electrons. This result may seem surprising, however, one must remember that the use of a reduced ion to electron mass ratio ($m_i/m_e < 1836$) produces larger drift velocities (and convection fluxes) than those applicable for a hydrogen ion.

6. Particle velocity distributions

The plots of Figs. 3 and 4 represent the velocity distributions of the electrons and ions within the source region (I), the source-free region (II), and the collector sheath region (III). The electron contour plots exhibit nearly Maxwellian (semicircular) behavior, except for the truncation of left-going particles (those with negative velocities), which becomes more pronounced as one approaches the plate. This

structure is due to the loss of high-energy electrons across the collector sheath to the plate, and the reflection of lower energy particles by the sheath. The ion contour plots indicate that the entire population of ions is accelerated toward the plate by the presheath and collector sheath potential drops. This is illustrated by the shift of the peak density location away from $v_\parallel = 0$ in region I, which increases as one approaches the plate.

C. The collisional dependence of particle and energy transport

1. The Coulomb collisional mean-free path

The variation of the collisional mean-free path (λ) with Coulomb collisionality is illustrated in Fig. 5, where λ is normalized by either the temperature or potential scale lengths [L_T or $L_\phi \equiv |(1/\phi)(\partial\phi/\partial z)|^{-1}$]. The collisionality increases from left to right in the figure. Classical transport theory is only valid within the shaded region of the figure, i.e., $0 \leqslant \lambda/L_T \leqslant 0.1$. The values of λ/L_T and λ/L_ϕ obtained from kinetic PIC simulations with $v^* \lesssim 0.5$ fall outside of this region. Therefore predictions of particle and energy transport obtained from the classical theory may be inaccurate in the low to moderately collisional regime $0.01 \leqslant v^* \lesssim 0.5$.

2. Ion flow energy

The ion flow energy along the spatial coordinate is shown as a function of collisionality in Fig. 6. The flow energy of species s is proportional to the square of the drift (flow) velocity ($\langle v_x \rangle$), which is defined as the normalized first moment of the distribution function

$$\langle v_x(z) \rangle \equiv \frac{1}{n_s(z)} \int_{v'=-\infty}^{\infty} v' f_s(z,v') d^3v', \qquad (14)$$

where the normalization factor is the species density n_s,

$$n_s(z) \equiv \int_{v'=-\infty}^{\infty} f_s(z,v') d^3v'. \qquad (15)$$

In the figure, the ion flow energy ($\epsilon_{\parallel,i} \equiv \frac{1}{2}m_i \langle v_{\parallel,i}^2 \rangle$) is normalized by either (i) the warm-ion acoustic flow energy
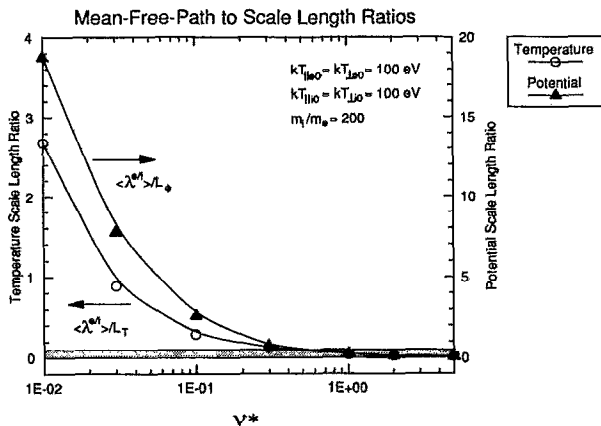
Mean-Free-Path to Scale Length Ratios

FIG. 5. The variation of the collisional mean-free path with Coulomb collisionality over the range $0.01 < v^* < 5.0$. Classical transport theory is valid within the shaded region $0 \leqslant \lambda/L_i \leqslant 0.1$.
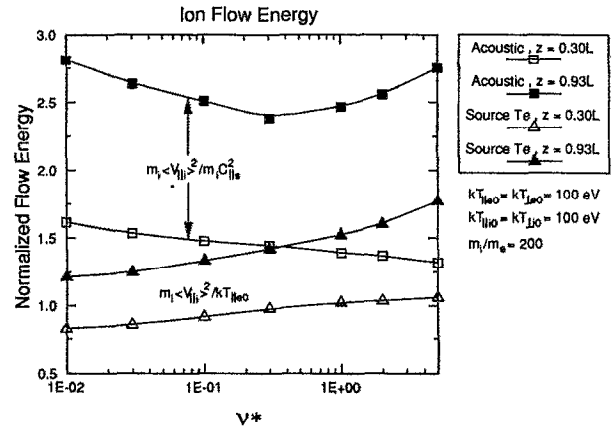
Ion Flow Energy

FIG. 6. The variation of the ion flow energy with Coulomb collisionality over the range $0.01 \leqslant v^* \leqslant 5.0$. The ion flow energy is normalized by either the warm-ion acoustic flow energy or the parallel electron source temperature.

$\frac{1}{2}m_i C_{\parallel,s}^2$ (squares), where the warm-ion acoustic velocity is defined as

$$C_{\parallel,s}(z) \equiv \{[kT_{\parallel,e}(z) + kT_{\parallel,i}(z)]/(m_e + m_i)\}^{1/2}, \qquad (16)$$

with $kT_{\parallel,e}(z)$ and $kT_{\parallel,i}(z)$ the local, equilibrium values of the parallel electron and ion temperatures; or (ii) the cold-ion acoustic flow energy $\frac{1}{2}m_i C_{\parallel,s}'^2$ (triangles), where the cold-ion, isothermal-electron acoustic velocity is given by

$$C_{\parallel,s}' \equiv (kT_{\parallel,e0}/m_i)^{1/2}, \qquad (17)$$

with $kT_{\parallel,e0}$ the parallel, source electron temperature. The open markers represent values measured at the edge of the distributed source region ($z = L_S = 0.30L$) and the filled markers are values measured at the interface between the quasineutral plasma and non-neutral collector-sheath regions ($z = 0.93L$).

The ion flow energy is found to increase with collisionality when normalized by the cold-ion, isothermal-electron acoustic flow energy, and decrease (at least at $z = 0.30L$) when normalized by the local, warm-ion acoustic flow energy. When normalized by the warm-ion acoustic velocity, the ion drift velocity is found to be supersonic ($\langle v_{\parallel,i} \rangle/C_{\parallel,s} > 1$) prior to reaching $z = L_S$, and remains supersonic all the way to the plate. Using the cold-ion, isothermal-electron acoustic velocity for normalization one finds that supersonic flow ($\langle v_{\parallel,i} \rangle/C_{\parallel,s}' > 1$) exists at $z = L_S$ only for moderate to high collisionalities. The Bohm sheath criterion[33] (which states that the ions must enter the collector sheath region with a velocity greater than the acoustic velocity, in order to maintain a stable, monotonically decreasing potential structure) is apparently satisfied in these simulations for either definition of the acoustic velocity.

3. Average ion impact kinetic energy

The average kinetic energy of the ions striking the plate is plotted as a function of collisionality in Fig. 7. The kinetic energy of species s (ϵ_s) is the second moment of the distribu-
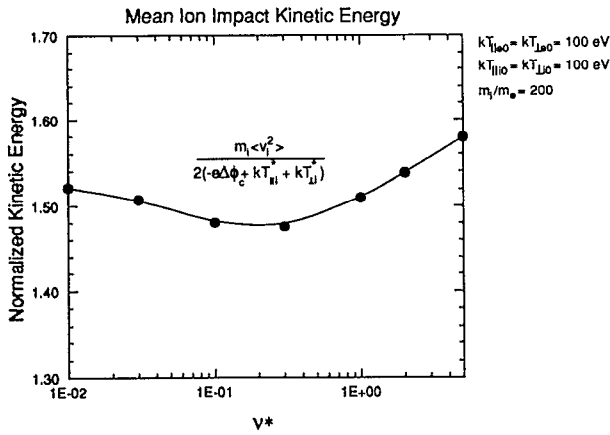
FIG. 7. The average ion kinetic energy at the plate as a function of Coulomb collisionality over the range $0.01 \leqslant v^* \leqslant 5.0$.

tion function

$$\epsilon_s(z) \equiv \frac{1}{n_s(z)} \int_{v'=-\infty}^{\infty} \frac{m_s v'^2}{2} f_s(z,v') d^3v'. \qquad (18)$$

The kinetic energy of the ions at the plate is normalized by the sum of their thermal energy at the plasma–sheath interface $kT^*_{\parallel,i} + kT^*_{\perp,i}$ and the energy gained through the acceleration by the collector sheath potential drop $-e\Delta\phi_c$. The figure shows that the average impact energy is about 50% larger than the value that is commonly used to determine whether or not the threshold for sputtering of the plate has been exceeded.

4. Plasma temperature

The collisional dependence of the equilibrium electron and ion temperatures are shown in Fig. 8. The d th component of the temperature ($T_{d,s}$), which is the variance of the second moment of the distribution function, is defined by

$$T_{d,s}(z) \equiv m_s \langle (v_d - \langle v_{d,s} \rangle)^2 \rangle$$

$$= \frac{1}{n_s(z)} \int_{v'=-\infty}^{\infty}$$

$$\times m_s (v_d'^2 - \langle v_{d,s} \rangle^2) f_s(z,v') d^3v'. \qquad (19)$$

Squares (triangles) represent the parallel (perpendicular) components of temperature. The circle markers located at $v^* = 0.01$ represent the values of the parallel temperature obtained from collisionless simulations, in which a refluxing algorithm is used to bring the system to steady state. (The refluxing process repopulates the truncated tail of the electron velocity distribution by replacing the energy of a particle with a value chosen from a Maxwellian at the source temperature, whenever the particle is reflected at $z = 0$. See Ref. 34 for a detailed discussion on the use of refluxing in PIC simulations.) Once again, the open markers are measured at $z = L_S = 0.30L$ and the closed markers are measured at the $z = 0.93L$.

The equilibrium parallel temperatures obtained from the collisionless simulation (in which the particle kinetic energy is *not* conserved due to the refluxing process) are considerably larger than those from the self-consistent colli-
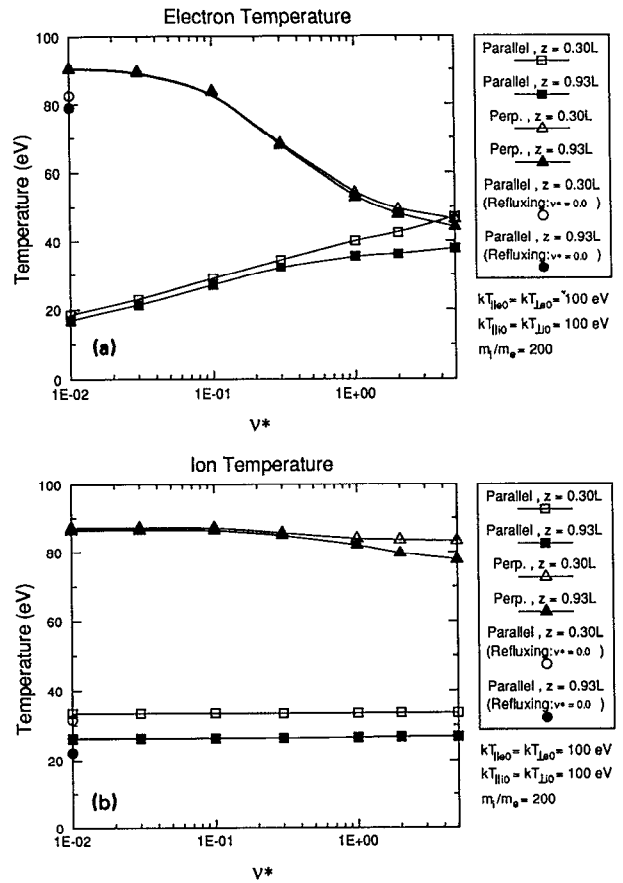
FIG. 8. The variation of the components of (a) the electron temperature and (b) the ion temperature with Coulomb collisionality over the range $0.01 \leqslant v^* \leqslant 5.0$.

sional simulations. This discrepancy illustrates a significant shortcoming of the collisionless PIC model of plasma transport. The parallel electron temperature [see Fig. 8(a)] exhibits an increase of 15 to 20 eV as the collisionality is increased, while the perpendicular electron temperature decreases by about 45 eV. The parallel electron temperature gradient, which transports particles and energy along the field lines, is found to increase with collisionality, as evidenced by the increasing separation between the square markers from left to right in Fig. 8(a). The components of the ion temperature show little dependence on collisionality [see Fig. 8(b)]. The nearly constant parallel ion temperature gradient is a consequence of the acceleration of ions by the presheath potential, a process that dominates the collisional transfer of energy from the ions to the electrons. Based upon these observations, it is reasonable to conclude that the collisional transfer of energy from the perpendicular to the parallel component of electron temperature is the main process that repopulates the tail of the truncated electron velocity distribution, thereby allowing the system to come to equilibrium.

5. Total kinetic energy flux

The steady-state values of the total kinetic energy flux of the electrons and ions are plotted as a function of Coulomb collisionality in Fig. 9. The kinetic energy flux (q^s_{tot}), which
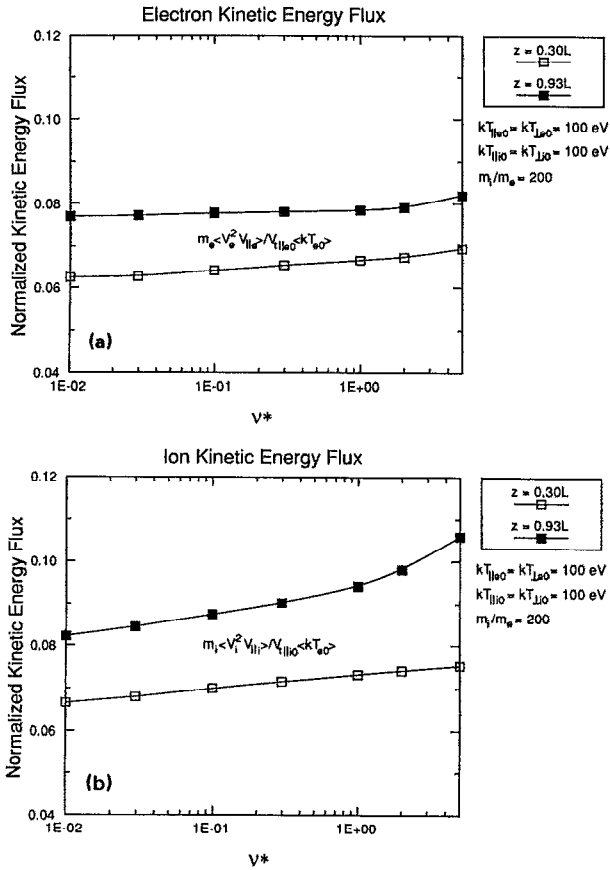
Electron Kinetic Energy Flux

Ion Kinetic Energy Flux

FIG. 9. The variation of (a) the electron and (b) the ion total kinetic energy flux with Coulomb collisionality over the range $0.01 \leqslant \nu^* \leqslant 5.0$.

includes contributions from both conductive and convective processes, is the third moment of the distribution function,

$$q_{tot}^s(z) \equiv m_s \langle v_s^2 v_{\parallel,s} \rangle$$
$$= \int_{v'=-\infty}^{\infty} v_{\parallel}' \frac{m_s v'^2}{2} f_s(z,v') d^3 v', \qquad (20)$$

where $v^2 = v_{\parallel}^2 + v_{\perp}^2$. The values of the kinetic energy flux presented in the figure are normalized by the source-electron free-streaming thermal flux $q_{fs}^e \equiv n_e v_{t\parallel,e0} kT_{e0}$. The kinetic energy flux of both species are shown in Fig. 9 to increase with collisionality. The electrons exhibit a relatively uniform increase in the kinetic energy flux between locations $z = 0.30L$ and $z = 0.93L$ over a wide range of collisionality. The difference in the ion kinetic energy flux between locations $z = 0.30L$ and $z = 0.93L$ increases with collisionality [see Fig. 9(b)], due to an increase in the convection heat flux, which in turn is associated with an increase in the drift velocity (see Fig. 6).

6. Sheath energy transmission factors

The sheath energy transmission factors of the electrons and ions are presented in Fig. 10 as a function of collisionality. The transmission factors are defined as the ratio of the total kinetic energy flux at the plasma-sheath interface to the ion flow energy at that location,

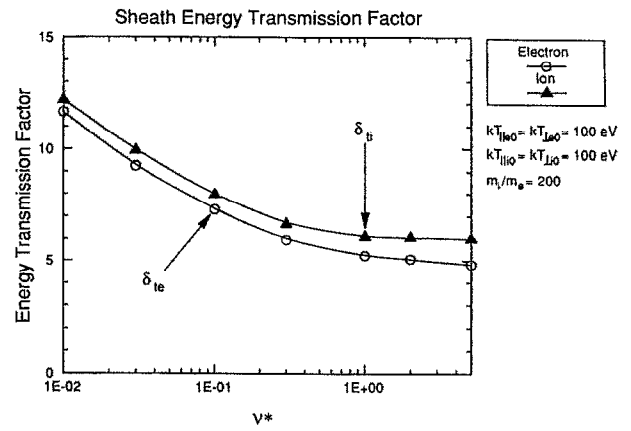$$\delta_{ts} \equiv q_{tot}^s(z=0.93L)/kT_{\parallel,e}^* \Gamma_{\parallel,i}^*, \qquad (21)$$

Sheath Energy Transmission Factor

FIG. 10. The variation of the electron and ion sheath energy transmission factors with Coulomb collisionality over the range $0.01 \leqslant \nu^* \leqslant 5.0$.

where kT_c^* is the electron temperature, $\Gamma_{\parallel,i}^* \equiv n_i^* \langle v_{\parallel,i} \rangle$ is the ion flux at the plasma-sheath interface. This quantity is used to describe the total kinetic energy flux of the species s at the plate, based upon the total energy flux at the plasma-sheath interface. The transmission factors for both species are shown to decrease with increasing collisionality.

7. Plasma heat conduction

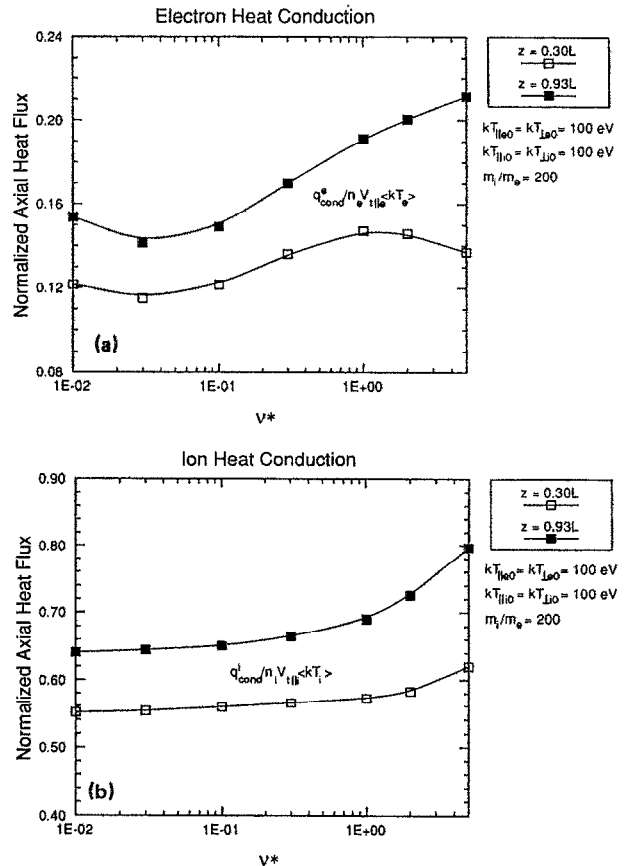The collisional dependence of the electron and ion heat conduction flux is shown in Fig. 11. The conduction flux

Electron Heat Conduction

Ion Heat Conduction

FIG. 11. The variation of (a) the electron and (b) the ion heat conduction flux with Coulomb collisionality over the range $0.01 \leqslant \nu^* \leqslant 5.0$.

(q_{cond}^s) is obtained from the total kinetic energy flux via the relation

$$q_{cond}^s(z) \equiv q_{tot}^s(z) - q_{conv}^s(z)$$

$$= \int_{v'=-\infty}^{\infty} (v_\parallel' - \langle v_{\parallel,s}\rangle)\frac{m_s v'^2}{2} f_s(z,v')d^3v', \tag{22}$$

where the convection flux (q_{conv}^s) is defined by

$$q_{conv}^s(z) = \int_{v'=-\infty}^{\infty} \langle v_{\parallel,s}'\rangle \frac{m_s v'^2}{2} f_s(z,v')d^3v', \tag{23}$$

with $\langle v_{\parallel,s}\rangle$ defined by (14). The values of the heat conduction flux presented in the figure are normalized by the local free-streaming thermal flux $q_{fs}^s(z) \equiv n_s(z)v_{\parallel,ts}(z)kT_s(z)$. The heat conduction flux of both species tends to increase with collisionality. The measured electron heat conduction flux [see Fig. 11(a)] is in the range of 12% to 21% of the free-streaming flux. Similarly, the ion conduction flux [see Fig. 11(b)] is limited to 55% to 80% of the free-streaming flux.

8. The electrostatic potential

The dependence of the various components of the total potential drop on collisionality is shown in Fig. 12. The
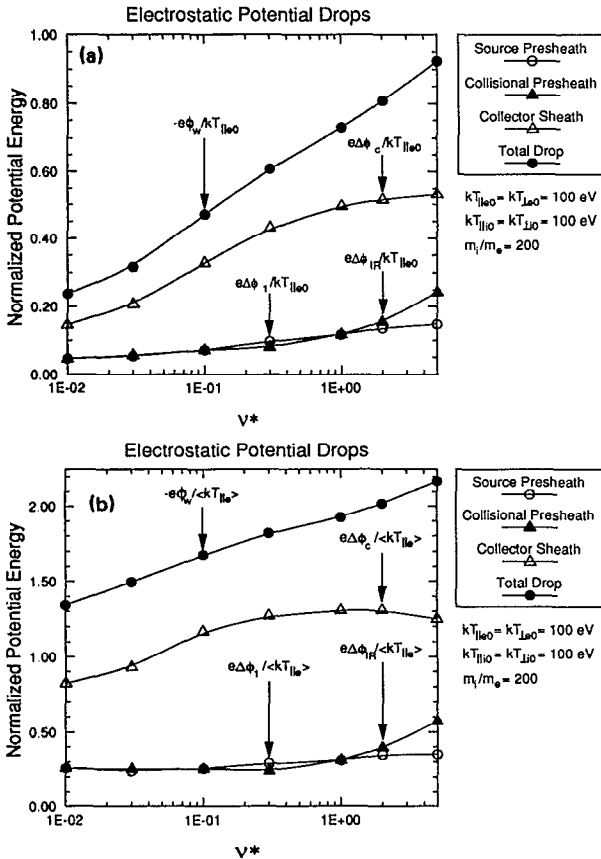

FIG. 12. The collisional dependence of the electrostatic potential energy drops, as normalized by (a) the parallel electron source temperature and (b) the parallel electron temperature at equilibrium, for collisionalities in the range $0.01 \leqslant \nu^* \leqslant 5.0$.

source presheath $(\Delta\phi_1)$, collisional presheath $(\Delta\phi_{IR})$, collector sheath $(\Delta\phi_c)$, and total potential (ϕ_w) energies are normalized by the parallel source electron temperature in Fig. 12(a), and by the parallel equilibrium electron temperature (which is averaged over the system length) in Fig. 12(b). The general trend observed in these figures is an increase in the potential drops with collisionality. Both the source and collisional presheath potential drops exhibit modest increases $[\delta(e\Delta\phi_1) \simeq 0.1kT_{\parallel,e0}, \delta(e\Delta\phi_{IR}) \simeq 0.2kT_{\parallel,e0}]$ as the collisional mean-free path decreases (for a fixed system length) from $\lambda = 100L$ $(\nu^* = 0.01)$ to $\lambda = 0.2L$ $(\nu^* = 5)$. The increasing presheath drops, in conjunction with the increasing parallel electron temperature gradient [see Eqs. (3)–(5), and Fig. 8(a)], support the increasing flow velocities or currents (shown in Fig. 6) and heat conduction fluxes (see Fig. 11). The increase in the collector sheath potential drop $[\delta(e\Delta\phi_c) \simeq 0.4kT_{\parallel,e0}]$ is associated with the increase in the parallel electron temperature at equilibrium, as shown in Fig. 8(a), since the two quantities are linearly related. The total potential drop ϕ_w is found to be in the range $1.341\langle kT_{\parallel,e}\rangle \lesssim -e\phi_w \lesssim 2.169\langle kT_{\parallel,e}\rangle$ for a mass ratio of $m_i/m_e = 200$. If one assumes that the collector sheath drop is logarithmically related to the mass ratio via $e\Delta\phi_c/kT_{\parallel,e}^* \sim \frac{1}{2}\ln(m_i/m_e)$ (which will be derived below), the total potential drop for a hydrogen $(_1H^1)$ plasma with mass ratio $m_H/m_e = 1836$ would vary between $2.403\langle kT_{\parallel,e}\rangle \lesssim -e\phi_w \lesssim 3.157\langle kT_{\parallel,e}\rangle$, while a plasma that consists of equal fractions of deuterium $(_1D^2)$ and tritium $(_1T^3)$ with an average mass ratio $m_{D-T}/m_e = 4590$ would have a total drop in the range $2.841\langle kT_{\parallel,e}\rangle \lesssim -e\phi_w \lesssim 3.565\langle kT_{\parallel,e}\rangle$.

V. COMPARISON WITH THE RESULTS OF OTHER PLASMA TRANSPORT MODELS

Selected results from the previous section are compared with the results of other plasma transport models.

A. Plasma density

The spatial profiles of the electron and ion densities that are given in Fig. 2(b) are similar to the profiles presented in Fig. 2(b) of Takizuka et al.,[27] which are for a system of length $L = 100\lambda_{De0}$, with a distributed-source region of width $L_S = 0.30L$, a mass ratio $m_i/m_e = 400$, and a source temperature ratio $T_{e0}/T_{i0} = 1$. Each model uses a Monte Carlo, binary particle collision algorithm within a code that is based upon the PIC methodology. A major difference lies in the implementation of the models: Takizuka et al. use only $N_{cell} \simeq 12$, whereas this study used $N_{cell} \simeq 100$ particles per cell. Each model predicts that the electron (ion) density at the plate is reduced to approximately 25% (50%) of the value at the plasma–sheath interface, such that the ion density is roughly twice as large as the electron density at the plate.

B. Ion flow energy

The spatial profiles of the electron and ion flow velocities plotted in Fig. 2(c) closely resemble those calculated by the PIC models of Takizuka et al. [see Fig. 2(c) of Ref. 27]

and Chodura,[28] and is similar to the fluid model results presented by Chodura [see Fig. 16(b) of Ref. 35]. Chodura's kinetic PIC model includes Coulomb collisions by allowing individual particles to interact with a background Maxwellian plasma at the local temperature. This scheme does not necessarily conserve the momentum or kinetic energy of the interacting particles. Each of the PIC models predicts a large increase in the electron drift velocity in the collector sheath region as the energetic electrons overcome the sheath potential barrier and flow to the plate. Chodura's one-dimensional fluid model, which simulates plasma transport in the source region (I) and source-free region (II), is based upon a static ($\partial /\partial t = 0$), quasineutral ($n_e = Zn_i$) implementation of the hydrodynamic transport equations (6). Although the fluid model uses a different form of the particle injection profile $h(z)$ than that employed in the present model, each of the flow velocity profiles exhibit a rapid increase within the source region (from zero at the midplane), followed by a gradual increase toward the plate within the source-free region. The results of Chodura's kinetic and fluid modeling indicate that the flow is supersonic by the time it reaches the interface between the source region (I) and the source-free region (II), which agrees with the data shown in Fig. 6 above (open, square markers).

The collisional dependence of the ion flow energy shown in Fig. 6 is similar to the results presented in Fig. 4 of Takizuka et al. Their results indicate that the flow is subsonic [when normalized by the local, warm-ion acoustic velocity $C_{\parallel,s}(z)$] at the edge of the source region ($z = 0.30L$), except at $v^* = 0.01$, where the Mach number is slightly larger than unity. While both sets of data for $z = 0.30L$ decrease with increasing collisionality, the results presented herein are supersonic over the entire range of collisionality $0.01 \leqslant v^* \leqslant 5$. Each model predicts that the ion flow velocity is supersonic at the entrance to the collector sheath region ($z = 0.95L$), when normalized by $C_{\parallel,s}(z)$. When normalized by the cold-ion, isothermal-electron acoustic velocity $C'_{\parallel,s}$, Takizuka et al. find that the flow is subsonic for $v^* \lesssim 1$, while the results from this study show the flow to be supersonic over the entire range of collisionality. Each of these kinetic models predicts that the flow at that location increases with collisionality, but the model of Takizuka et al. gives values for the flow energies that are between 11.6% and 56.4% smaller than the values obtained in the present study. The discrepancies between the results of these two kinetic models can lead to different conclusions regarding the applicability of the Bohm sheath criterion to a bounded, collisional plasma system. It should also be pointed out that many fluid transport models[13,36,37] impose a sonic flow boundary condition ($\langle v_\parallel \rangle = C_{\parallel,s}$) at the plasma–sheath interface, in accordance with the Bohm sheath criterion. This practice is open to question in light of the results presented in Fig. 6, which indicate that the flow at that location is supersonic by 11.0% to 65.9%, depending upon the collisionality and the definition of the sound speed.

C. Plasma temperature

The profiles of the parallel temperature of the electrons and ions that are predicted by the kinetic models of Chodura

and Takizuka et al. [see Fig. 2(f) of Ref. 27], and the fluid model of Chodura [see Fig. 16(b) of Ref. 35] are similar to those plotted in Fig. 2(d). The parallel ion temperature (which is only presented for the kinetic models) exhibits a sharp drop near the edge of the distributed source region, becoming relatively constant in the source-free region, with an additional decrease in the collector sheath region as the ions are accelerated by the decreasing potential structure. The parallel electron temperature decreases slowly through the source and source-free regions, and (for the kinetic models only) more rapidly in the collector sheath region. The reduction of the parallel component of the electron and ion temperatures within the collector sheath region is also in agreement with the collisionless, analytic theory of Schwager and Birdsall.[29] The spatial profiles of perpendicular temperature calculated by Takizuka et al. [see Fig. 2(e) of Ref. 27] and those obtained in the present study [see Fig. 2(d) above] are relatively flat.

Takizuka et al. predict that the parallel (perpendicular) component of the electron temperature increases (decreases) with increasing collisionality, such that the two components of the temperature are equal for $v^* \simeq 1.5$ [see Fig. 5(a) of Ref. 27]. The results from the present study, which give equal contributions to the total electron temperature for $v^* \simeq 5$ [see Fig. 8(a)], are in reasonable agreement with those of Takizuka et al. Their model gives equilibrium parallel and perpendicular electron temperatures for $v^* = 1$ of $kT_{\parallel,e} \simeq 0.32kT_{\parallel,e0}$ and $kT_{\perp,e} \simeq 0.34kT_{\perp,e0}$ (for $m_i/m_e = 400$), whereas the model used for this study gives $kT_{\parallel,e} \simeq 0.38kT_{\parallel,e0}$ and $kT_{\perp,e} \simeq 0.54kT_{\perp,e0}$ (for $m_i/m_e = 200$). The collisional dependence of the perpendicular ion temperature [shown in Fig. 8(b) above and Fig. 5(b) of Ref. 27] is similar for each model. The model of Takizuka et al. predicts that the parallel ion temperature increases by $\sim 0.15kT_{\parallel,e0}$ as the collisionality is increased from $v^* = 0.01$ to $v^* = 10$. In contrast to their results, the present study suggests that the parallel ion temperature increases only slightly with collisionality [see Fig. 8(b)], a trend that is barely noticeable above the level of statistical fluctuations. The exact reason for the discrepancy between the results from the two PIC models is not understood. However, the results of the present study had a lower level of statistical fluctuations than those presented in Ref. 27 (see Sec. IV A). Furthermore, the results presented by Takizuka et al. for the parallel electron temperature at $z = 0.95L$ and the collector sheath drop are inconsistent for $v^* \gtrsim 1$ (as discussed in Sec. V G). It is possible that this inconsistency is due to the large level of statistical fluctuations of the potential in their simulations. The increase in the parallel ion temperature with collisionality noted by Takizuka et al. may also arise from these fluctuations, which tend to diffuse particles in velocity space (i.e., heat the particles).

D. Total kinetic energy flux

The spatial profiles of the total kinetic energy flux predicted by Chodura's kinetic[28] and fluid models [see Fig. 16(b) of Ref. 35] are in good agreement with the data presented in Fig. 2(e) above, where the total kinetic energy flux is the sum of the conduction and convection fluxes. The ki-

1886   Phys. Fluids B, Vol. 3, No. 8, August 1991

R. J. Procassini and C. K. Birdsall   1886

TABLE II. Electron sheath energy transmission factors from simulations and theory for $m_i/m_e = 200$ and various collisionalities v^*. (Percent differences from the simulation results are shown in parentheses.)

$v^* \equiv v_{c0}/v_{be0}$	Simulation	Theoretical models			
		I-a	I-b	II-a	II-b
0.01	11.626	2.859	3.263	7.171	7.594
		(−75.4%)	(−71.9%)	(−38.3%)	(−34.7%)
0.1	7.291	3.206	3.392	5.279	5.466
		(−56.0%)	(−53.5%)	(−27.6%)	(−25.0%)
1	5.222	3.390	3.452	3.876	3.938
		(−35.1%)	(−33.9%)	(−25.8%)	(−24.6%)

netic energy flux rises rapidly within the source region (from zero at the midplane), and is constant (within the statistical fluctuation level) in the source-free and collector sheath regions.

The results of this study indicate that the electron total kinetic energy flux at $z = 0.30L$ ($z = 0.93L$) increases monotonically from 6.2% to 6.9% (7.7% to 8.2%) of the source kinetic energy flux, as the collisionality is increased from $v^* = 0.01$ to $v^* = 5$ [see Fig. 9(a)]. The same quantity is presented in Fig. 8.b-1 of Takizuka et al. at $z = 0.30L$ ($z = 0.95L$), showing an increase from 1.7% to 2.8% (2.3% to 3.8%) for $0.01 \leqslant v^* \leqslant 10$. Their normalized kinetic energy flux does not increase monotonically with collisionality, but instead has a peak value of 3.6% (4.3%) for $v^* = 1$. The collisional plasma system with a mass ratio of $m_i/m_e = 200$ is apparently able to transport a larger fraction of the kinetic energy that is injected into the system in the source region, than the system with a mass ratio of $m_i/m_e = 400$.

E. Sheath energy transmission factors

The values of the sheath energy transmission factors shown in Fig. 10 may be compared with those obtained from simple analytic models of the energy balance in the collector sheath region.[38,39] These models, which assume that the ions at the entrance to the collector sheath region ($z = z^*$) have a drift velocity $\langle v_{\parallel,i} \rangle^* \simeq C_{\parallel,s}^*$, define the energy transmission factors as

$$\delta_{te} \equiv q_{tot}^e(z^*)/kT_{\parallel,e}^* \Gamma_i^* = 2 - \psi_f, \quad (24)$$

$$\delta_{ti} \equiv q_{tot}^i(z^*)/kT_{\parallel,e}^* \Gamma_i^* = 2(kT_{\parallel,i}^*/kT_{\parallel,e}^*), \quad (25)$$

where $\psi_f \equiv e \, \Delta\phi_c/kT_{\parallel,e}^*$ is the normalized potential energy associated with traversing the collector sheath region, and the factors of 2 in (24) and (25) result from the assumption of isotropic temperatures at the plasma–sheath interface, i.e., $kT_{\parallel,s}^* = kT_{\perp,s}^*$. These expressions provide an estimate of the total kinetic energy flux that is incident upon the plate. The collector sheath potential energy is added to the electron thermal energy flux since the only electrons that will be incident upon the plate are those with energies greater than the sheath potential barrier. A more accurate model can be developed, which accounts for the anisotropies in the plasma temperature that result from the interaction of the plasma with the electrostatic potential

$$\delta_{te} = 1 + kT_{\perp,e}^*/kT_{\parallel,e}^* - \psi_f, \quad (26)$$

$$\delta_{ti} = (kT_{\parallel,i}^* + kT_{\perp,i}^*)/kT_{\parallel,e}^*. \quad (27)$$

The values of the sheath energy transmission factors shown in Fig. 10 will now be compared with those from each model for a mass ratio of $m_i/m_e = 200$. The isotropic temperature model given by Eqs. (24) and (25) will be termed model I, while the anisotropic model given by Eqs. (26) and (27) will be termed model II. The value of the normalized sheath potential energy ψ_f used in (24) and (26) is either measured from the simulations (models I-a and II-a) or obtained from the model of Stangeby,[38]

$$\psi_f = \frac{1}{2} \ln\left[\left(\frac{2\pi m_e}{m_i}\right)\left(1 + \frac{kT_{\parallel,i}^*}{kT_{\parallel,e}^*}\right)\right] \quad (28)$$

(models I-b and II-b). The value of the temperature ratios used in Eqs. (25)–(28) are obtained from the simulations. The measured and predicted values of the sheath energy transmission factors for $v^* = 0.01, 0.1$, and 1 are compared in Table II for the electrons and Table III for the ions.

The electron transmission factors obtained from the PIC simulations are at least ~25% larger than those obtained from either theoretical model. The anisotropic model gives electron transmission factors that are in better agreement with the simulations than does the isotropic model (see Table II). The agreement between the theoretical and simulation models is best for highly collisional plasmas, and falls off as the collisionality is decreased. The anisotropic model also gives ion energy transmission factors that are in better agreement with the simulations than those from the isotrop-

TABLE III. Ion sheath energy transmission factors from simulations and theory for $m_i/m_e = 200$ and various collisionalities v^*. (Percent differences from the simulation results are shown in parentheses.)

$v^* \equiv v_{c0}/v_{be0}$	Simulation	Theoretical models	
		I	II
0.01	12.270	3.094	6.635
		(−74.8%)	(−45.9%)
0.1	7.960	1.934	4.147
		(−75.7%)	(−47.9%)
1	6.086	1.489	3.056
		(−75.5%)	(−49.8%)

ic model (see Table III). The agreement between the ion transmission factors obtained from the theory and simulations shows little or no collisional dependence. Note that the values of the ion (and electron) flow velocity measured at the entrance to the collector sheath region exceed the local acoustic velocity by 11.0% to 65.9%, depending upon the definition of the acoustic velocity (see Fig. 6), while the theories assume sonic flow at that location. In addition, the measured kinetic energy of the flowing plasma is larger than its temperature (as evidenced by the data shown in Fig. 7), while the theories normalize the total kinetic energy flux by the electron temperature. Each of these differences leads to measured sheath transmission factors from the simulations that are larger than those predicted by the theories.

F. Plasma heat conduction

The electron conduction heat fluxes obtained from the PIC simulations and classical transport theory are compared in Fig. 13. The classical description of parallel heat conduction for species s is given by

$$q_{cl,cond}^s = -\kappa_\parallel^s \nabla_\parallel T_s. \tag{29}$$

The parallel electron thermal conductivity is defined by[8]

$$\kappa_\parallel^e = 3.2(n_e kT_e \tau_{90}^{e/e}/m_e), \tag{30}$$

where the electron 90° scattering time $\tau_{90}^{e/e} = 0.70\tau_0$. The parallel gradient of the electron temperature that is used in (29) is obtained from the simulations.

For nonzero values of the collisional mean-free-path λ (or finite values of the collisionality ν^*), Fig. 13 indicates that the average thermal conductivity along the spatial coordinate is reduced relative to the value predicted by classical transport theory. This result is in agreement with the Monte Carlo simulations of thermal transport that were performed by Kahn and Rognlien,[40] and by Rognlien.[32] These Monte Carlo models follow the trajectories of individual electrons as they scatter off of a background plasma that is assumed to have a Maxwellian velocity distribution at a given temperature. The electron conduction heat flux is found to be limited to ~10%–20% of the free-streaming thermal flux over a

wide range of collisionality [see Fig. 11(a)]. These values of the heat flux limit are in agreement with the results presented by Rognlien[32] for the transport of energy in a tokamak scrapeoff layer, and by Luciani et al.,[41] who employ a nonlocal macroscopic expression of the heat conduction flux to study thermal transport in laser-produced plasmas.

G. The electrostatic potential

The spatial profiles of the electrostatic potential that are presented by Takizuka et al. [see Fig. 2(a) of Ref. 27] and Chodura[28] agree reasonably well with the potential profile plotted in Fig. 2(a) above. In each case, the presheath potential drop is the sum of the source sheath drop $\Delta\phi_1$ in the distributed source region and the collisional sheath drop $\Delta\phi_{IR}$ in the source-free region. The collector sheath drop $\Delta\phi_c$ forms over the region approximately $5\lambda_{De}$ wide adjacent to the plate.

The collisional sheath drop $\Delta\phi_{IR}$ calculated by Takizuka et al. is found to increase with collisionality (see Fig. 3 of Ref. 27). This trend agrees with the results from the present study, which are plotted in Fig. 12. However, this is not true of the results presented by Scheuer and Emmert, which show little or no change in the potential at the plasma-sheath interface as the collisional mean-free path is varied over two orders of magnitude (see the results for case 3 plotted in Fig. 8 of Ref. 42). Note that their normalized collisional mean-free path is equal to the reciprocal of the collisionality, since $\delta \equiv \lambda/L = (v_t/v_c)/L = v_b/v_c = 1/\nu^*$. Their analytic theory includes a Bhatnagar–Gross–Krook (BGK) collision term in the ion Boltzmann equation, and uses a Boltzmann relation for the electron density $\{n_e(x) = \exp[e\phi(x)/kT_e]\}$. For this reason, only ion–ion collisions are included in their model.

The collisional dependence of the collector sheath drop is also an area where different results are obtained from these three models. Once again, the results obtained by Scheuer and Emmert show little variation of the total potential drop with ion–ion collisionality (see Fig. 8 of Ref. 42). When coupled with their results for the presheath drop, one finds that the collector sheath drop is only slightly affected by the level of ion–ion collisionality. This weak collisional dependence is in general agreement with the data presented in Figs. 8, 9, and 12, which indicate that electron–electron (not electron–ion or ion–ion) collisions play a significant role in determining the structure of the electrostatic potential.

Figure 12(a) shows that the collector sheath drop increases monotonically with Coulomb collisionality, and begins to level off for $\nu^* \gtrsim 1$. Note that the parallel electron temperature at the plasma–sheath interface has a similar collisional dependence [see Fig. 8(a)]. Therefore these two sets of data are consistent, since the collector sheath drop is linearly proportional to the thermal spread of the electrons as they enter the sheath region. To illustrate this, consider the charge continuity equation for species s within a one-dimensional collector sheath region,

$$q_s \frac{\partial n_s}{\partial t} + \nabla \cdot \mathbf{J}_s = q_s S_s, \tag{31}$$
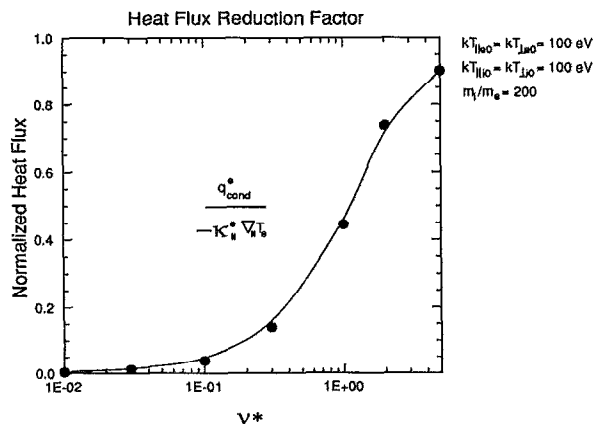

FIG. 13. A comparison of the average thermal conductivity along the spatial coordinate obtained from the PIC simulations and classical transport theory as a function of Coulomb collisionality.

where $\mathbf{J}_s = q_s \Gamma_s$ is the current, Γ_s is the particle flux, and S_s is the source rate. Assuming a steady-state solution of (31) with no sources in the sheath region, one obtains $\nabla \cdot \mathbf{J}_s = 0$, such that $\mathbf{J}_s$ is constant over the region. The charge on the surface of the plate is constant at equilibrium, which implies $\mathbf{J}_{tot}(L) \equiv \mathbf{J}_e(L) + \mathbf{J}_i(L) = 0$, or $\mathbf{J}_e(L) = -\mathbf{J}_i(L)$. The currents that are incident upon the plate may be modeled as

$$J_e(L) \equiv | -e|n_e^* \langle v_{\|,e} \rangle (L) \exp[e\,\Delta\phi_c / kT_{\|,e}(L)], \quad (32)$$

$$\simeq en_e^* v_{t\|,e}(L) \exp[e\,\Delta\phi_c / kT_{\|,e}(L)], \quad (33)$$

$$J_i(L) \equiv Zen_i^* \langle v_{\|,i} \rangle (L), \quad (34)$$

$$\simeq Zen_i^* \mathcal{M} C_{\|,s}, \quad (35)$$

where n_s^* is the density of species s at the entrance to the sheath region, $\mathcal{M}$ is the Mach number of the flow at the plate, $C_{\|,s}(L)$ is the acoustic velocity at the plate, and the exponential in (33) accounts for reduction of the electron density by the sheath potential barrier. The system is assumed to be quasineutral at the plasma–sheath interface, such that $n_e^* = n_i^*$. Using the warm-ion definition of the acoustic velocity $C_{\|,s} \equiv [(kT_{\|,e} + kT_{\|,i})/m_i]^{1/2}$, setting the thermal velocity to $v_{t\|,e} = (kT_{\|,e}/m_e)^{1/2}$, and equating (33) and (35), one obtains

$$\exp\left(\frac{e\,\Delta\phi_c}{kT_{\|,e}}\right) = Z\mathcal{M}\left(\frac{m_e}{m_i}\right)^{1/2}\left(1 + \frac{kT_{\|,i}(L)}{kT_{\|,e}(L)}\right)^{1/2}, \quad (36)$$

which may be arranged to give

$$\frac{e\,\Delta\phi_c}{kT_{\|,e}} = \frac{1}{2}\ln\left[(Z\mathcal{M})^2\left(\frac{m_e}{m_i}\right)\left(1 + \frac{kT_{\|,i}(L)}{kT_{\|,e}(L)}\right)\right]. \quad (37)$$

Therefore the simple relationship between the species currents at the plate provides an expression for the collector sheath potential drop, which varies linearly with parallel electron temperature and logarithmically with mass ratio. Similar expressions that include the same scaling with temperature and mass ratio have been developed by several researchers.[43,23,38,44]

Based upon these results, it is interesting to note the collisional dependence of the parallel electron temperature and the collector sheath drop that is obtained from the model of Takizuka et al. They report that the parallel electron temperature at the entrance to the collector sheath region ($z = 0.95L$) increases monotonically with collisionality, and levels off for $\nu^* \gtrsim 1$ [see Fig. 5(a) of Ref. 27]. On the other hand, the collector sheath drop is shown to increase with collisionality over the range $0.01 \leqslant \nu^* \lesssim 1$, and then decrease for larger values of ν^* (see Fig. 3 of Ref. 27). These two sets of data appear to be inconsistent with each other, especially since the right side of (37) is a slowly varying function of the Mach number $\mathcal{M}$ and the temperature ratio $T_{\|,i}(L)/T_{\|,e}(L)$. Since the simulations of Ref. 27 were performed with $N_{cell} \simeq 12$ particles per grid cell, it is possible that the large statistical fluctuations of the potential that are associated with such a small density of superparticles preclude them from obtaining an accurate measurement of the collector sheath potential drop. This may also be the reason for the previously observed discrepancies in other results obtained from the two models.

TABLE IV. Total potential drop ϕ_w from simulations and theory for several mass ratios m_i/m_e and collisionalities ν^*. (Percent differences from the theoretical results are shown in parentheses.)

m_i/m_e	Theory: $-e\phi_w/kT_{\|,e0}$ (Emmert et al.)	Simulations: $-e\phi_w/\langle kT_{\|,e}\rangle$	
		$\nu^* = 0.01$	$\nu^* = 5$
200	1.874	1.341 (-28.4%)	2.169 ($+15.7\%$)
1836	2.982	2.450 (-17.8%)	3.278 ($+9.9\%$)
4590	3.441	2.908 (-15.5%)	3.736 ($+8.6\%$)

The values of the total potential drops obtained from the simulations and the theory of Emmert et al. [using Eq. (35) of Ref. 23] will now be compared. The results from the simulations are normalized by the average of the parallel electron temperature along the field line, while the predictions from the theory are normalized by the parallel electron source temperature, which is assumed to be spatially constant. The temperature ratio $\langle kT_{\|,i}\rangle / \langle kT_{\|,e}\rangle$ that is measured from the simulations will be used in Emmert's analytic expression for $-e\phi_w/kT_{\|,e0}$. As shown in Fig. 12(b), the smallest and largest values of $-e\phi_w/\langle kT_{\|,e}\rangle$ obtained from the simulations occur at $\nu^* = 0.01$ and $\nu^* = 5$, respectively. Table IV shows the total potential drops obtained from the theory and simulations for mass ratios $m_i/m_e = 200$ (used in the present study), $m_H/m_e = 1836$ [for a hydrogen ($_1H^1$) plasma], and $m_{D-T}/m_e = 4590$ [for an equal-fraction plasma of deuterium ($_1D^2$) and tritium ($_1T^3$)]. The simulation results are extrapolated to larger mass ratios by assuming that the total potential drop has a logarithmic dependence on the mass ratio, as shown in (37). The results from the simulations are found to lie on either side of the analytic results, with the low- (high-)collisionality simulations yielding total drops that are smaller (larger) than those obtained from the theory of Emmert et al. The agreement between simulation and theory seems to improve with increasing mass ratio. This is not surprising, since Emmert's use of Boltzmann (inertialess) electrons implies an infinite ion to electron mass ratio. Note that while the analytic theory was derived for a collisionless system, the highly collisional simulation results are in better agreement with the theory than those from the low-collisionality simulation, which may seem counterintuitive. However, when the electrons are highly collisional, they better satisfy the assumption made by Emmert et al. that the electrons are Boltzmann at the source temperature.

VI. SUMMARY AND CONCLUSIONS

The collisional transport of particles and energy in a bounded plasma system has been investigated over a wide range of Coulomb collisionality. The particle simulation code DIPSI, which combines standard particle-in-cell (PIC) techniques with a Monte Carlo, binary-particle Coulomb collision algorithm, has been used to provide a self-consis-

tent, kinetic description of transport and potential formation in both the quasineutral portion of the plasma and the non-neutral collector sheath region adjacent to the bounding plate. Particles that are created in the distributed source region are followed as they flow to the plate, where they are absorbed on the surface of the floating conductor.

The results of each PIC simulation indicate that the ion flow velocity is supersonic (when compared with the local, warm-ion acoustic velocity) at the edge of the distributed source region ($z = L_S$), and hence farther downstream, as a result of the acceleration by the source sheath potential drop $\Delta\phi_1$. Therefore the Bohm criterion for the existence of a stable sheath was satisfied for all the simulations.

The parallel electron temperature at equilibrium was shown to increase with collisionality, at the expense of the perpendicular electron temperature. This collisional energy transfer allows electrons that were electrostatically trapped by the collector sheaths to overcome those potential barriers and exit the system via absorption at the plate. The collector sheath potential drop $\Delta\phi_c$ also increases with collisionality, a trend that is consistent with an increasing parallel electron temperature. The source sheath $\Delta\phi_1$ and collisional pre-sheath $\Delta\phi_{IR}$ drops, and thus the total potential drop ϕ_w also increases with collisionality.

Nonzero values of the collisional mean-free-path λ (which corresponds to finite collisionalities ν^*) give thermal conductivities that are reduced relative to the predictions of classical transport theory. This implies a concomitant reduction of the equilibrium parallel electron temperature at the entrance to the collector sheath region $kT^*_{\parallel,c}$. Since the collector sheath potential drop $\Delta\phi_c$ scales linearly with $kT^*_{\parallel,c}$, and the overall presheath drop $\Delta\phi_1 + \Delta\phi_{IR}$ falls off as the collisionality is decreased, the total potential drop ϕ_w for a finite mean-free-path plasma will be smaller than the value predicted by classical transport theory. The total potential drop ϕ_w is smaller (larger) than the value obtained from the analytic, collisionless plasma–sheath model of Emmert *et al.*[23] for low- (high-) collisionality plasmas.

The total kinetic energy flux of both the electrons and ions was found to increase with collisionality, while the sheath energy transmission factors of both species decrease as the system becomes more collisional. The energy transmission factors obtained from the simulation were consistently larger than the values obtained from a simple sheath energy-balance model. The electron and ion heat fluxes due to conduction generally increase with collisionality. The electron heat conduction flux q^e_{cond} was found to be limited to ~10%–20% of the free-streaming thermal flux $q^e_{fs} \equiv n_e v_{\parallel,te} kT_e$; a flux limit that agrees well with the results of other transport models.[32,41]

The particle simulation model used for this study has provided an accurate description of transport phenomena that arise from Coulomb collisions. One important aspect of collisional transport that was not included in the present study is the interaction of charged plasma particles with background neutral gas. These charged/neutral interactions, in the form of charge-exchange and impact-ionization events, have been included in a subsequent study of collisional plasma transport.[45]

ACKNOWLEDGMENTS

[1] S. A. Cohen and the ITER Team, Bull. Am. Phys. Soc. **34**, 1970 (1989).
[2] F. L. Hinton and G. M. Staebler, Nucl. Fusion **29**, 405 (1989).
[3] P. C. Stangeby, J. Phys. D **15**, 1007 (1982).
[4] P. C. Stangeby, Phys. Fluids **28**, 644 (1985).
[5] S. A. Cohen, in *Plasma Etching: An Introduction*, edited by D. M. Manos and D. L. Flamm (Academic, Boston, MA, 1989), pp. 217–219.
[6] A. Gras-Marti, J. A. Vallés-Abarca, and J. C. Moreno-Marin, in *Plasma–Surface Interactions and Processing of Materials*, NATO Advanced Studies Institute, Alicante, 1988 edited by O. Auciello, A. Gras-Marti, J. A. Vallés-Abarca, and D. L. Flamm (Kluwer Academic, Dordrecht, 1990), pp. 135–146.
[7] L. Spitzer and R. Härm, Phys. Rev. **89**, 977 (1953).
[8] S. I. Braginskii, in *Reviews of Plasma Physics* (Consultants Bureau, New York, 1965), Vol. 1, p. 205.
[9] F. L. Hinton and R. D. Hazeltine, Rev. Mod. Phys. **48**, 246, 261 (1976).
[10] E. Zawaideh, F. Najmabadi, and R. W. Conn, Phys. Fluids **29**, 463 (1986).
[11] J. T. Hogan, in *Methods in Computational Physics* (Academic, New York, 1976), Vol. 16, pp. 131–164.
[12] B. J. Braams, P. J. Harbour, M. F. A. Harrison, E. S. Hotston, and J. G. Morgan, J. Nucl. Mater. **121**, 75 (1984).
[13] N. Ueda, M. Kasai, M. Tanaka, M. Sugihara, and S. Sengoku, Nucl. Fusion **28**, 1183 (1988).
[14] R. S. Cohen, L. Spitzer, and P. M. Routly, Phys. Rev. **80**, 230 (1950).
[15] D. L. Flamm, in *Plasma Etching: An Introduction*, edited by D. M. Manos and D. L. Flamm (Academic, Boston, MA, 1989), pp. 92–95.
[16] J. M. E. Harper, in *Plasma–Surface Interactions and Processing of Materials*, NATO Advanced Studies Institute, Alicante, 1988, edited by O. Auciello, A. Gras-Marti, J. A. Vallés-Abarca, and D. L. Flamm (Kluwer Academic, Dordrecht, 1990), pp. 255–263.
[17] A. Gibson, J. Nucl. Mater. **76-77**, 92 (1978).
[18] V. A. Abramov, Y. L. Igitkhanov, V. I. Pistonuvich, and V. A. Pozharov, J. Nucl. Mater. **162-164**, 462 (1989).
[19] See AIP Document No. PAPS-PFBPE-03-1876-29 for 29 pages of "The DIPSI Computer Code User's Manual," Lawrence Livermore National Laboratory Report No. UCRL-ID 104093, 1990, by R. J. Procassini and B. I. Cohen. Order by PAPS number and journal reference from American Institute of Physics, Physics Auxiliary Publication Service, 335 East 45th Street, New York, NY 10017. The price is $1.50 for each microfiche (98 pages) or $5 for photocopies of up to 30 pages, and $0.15 for each additional page over 30 pages. Airmail additional. Make checks payable to the American Institute of Physics.
[20] R. J. Procassini, Ph.D. thesis, University of California, Berkeley, 1990.
[21] B. I. Cohen, A. B. Langdon, and A. Friedman, J. Comput. Phys. **46**, 15 (1982).
[22] A. B. Langdon, B. I. Cohen, and A. Friedman, J. Comput. Phys. **51**, 107 (1983).
[23] G. A. Emmert, R. M. Wieland, A. T. Mense, and J. N. Davidson, Phys. Fluids **23**, 803 (1980).
[24] J. T. Scheuer and G. A. Emmert, Phys. Fluids **31**, 3645 (1988).
[25] T. Takizuka and H. Abe, J. Comput. Phys. **25**, 205 (1977).
[26] L. Spitzer, in *Physics of Fully Ionized Gases*, 2nd ed. (Interscience, New York, 1962), pp. 120–127.

1890   Phys. Fluids B, Vol. 3, No. 8, August 1991

R. J. Procassini and C. K. Birdsall   1890

[27] T. Takizuka, K. Tani, M. Azumi, and K. Shimizu, J. Nucl. Mater. **128-129**, 104 (1984).

[28] R. Chodura, in *Controlled Fusion and Plasma Physics*, Proceedings of the 12th European Conference, Budapest, 1985 (European Physical Society, Geneva, 1985), Vol. 9F, Part II, p. 472.

[29] L. A. Schwager and C. K. Birdsall, Phys. Fluids B **2**, 1057 (1990).

[30] C. K. Birdsall and A. B. Langdon, in *Plasma Physics Via Computer Simulation* (McGraw-Hill, New York, 1985), pp. 293, 295–300.

[31] D. L. Flamm and G. K. Herb, in *Plasma Etching: An Introduction*, edited by D. M. Manos and D. L. Flamm (Academic, Boston, MA, 1989), pp. 17, 25.

[32] T. D. Rognlien, Bull. Am. Phys. Soc. **34**, 1981 (1989).

[33] D. Bohm, in *The Characteristics of Electrical Discharges in Magnetic Fields*, edited by A. Guthrie and R. K. Wakerling (McGraw-Hill, New York, 1949), p. 77.

[34] R. J. Procassini, C. K. Birdsall, and E. C. Morse, Phys. Fluids B **2**, 3191 (1990).

[35] R. Chodura, in *Physics of Plasma–Wall Interactions in Controlled Fusion*, edited by D. E. Post and R. Behrisch (Plenum, New York, 1986), p. 99.

[36] M. Petravic, D. Post, D. Heifetz, and J. Schmidt, Phys. Rev. Lett. **48**, 326 (1982).

[37] W. Schneider, D. B. Heifetz, K. Lackner, J. Neuhauser, D. E. Post, and K. G. Rauh, J. Nucl. Mater. **121**, 178 (1984).

[38] P. C. Stangeby, Phys. Fluids **27**, 682 (1984).

[39] R. C. Bissell, P. C. Johnson, and P. C. Stangeby, Phys. Fluids B **1**, 1133 (1989).

[40] S. A. Kahn and T. D. Rognlien, Phys. Fluids **24**, 1442 (1981).

[41] J. F. Luciani, P. Mora, and J. Virmont, Phys. Rev. Lett. **51**, 1664 (1983).

[42] J. T. Scheuer and G. A. Emmert, Phys. Fluids **31**, 1748 (1988).

[43] S. A. Self, Phys. Fluids **6**, 1762 (1963).

[44] R. C. Bissell and P. C. Johnson, Phys. Fluids **30**, 779 (1987).

[45] R. J. Procassini, C. K. Birdsall, and B. I. Cohen, Nucl. Fusion **30**, 2329 (1990).